



# Overcoming plasticity reduction in a severely deformed nano-grained metastable alloy

Yemao Lu, Gaoming Zhu, Horst Hahn & Yulia Ivanisenko

To cite this article: Yemao Lu, Gaoming Zhu, Horst Hahn & Yulia Ivanisenko (2024) Overcoming plasticity reduction in a severely deformed nano-grained metastable alloy, Materials Research Letters, 12:7, 525-534, DOI: [10.1080/21663831.2024.2356761](https://doi.org/10.1080/21663831.2024.2356761)

To link to this article: <https://doi.org/10.1080/21663831.2024.2356761>



© 2024 The Author(s). Published by Informa UK Limited, trading as Taylor & Francis Group



[View supplementary material](#)



Published online: 29 May 2024.



[Submit your article to this journal](#)



Article views: 329



[View related articles](#)



[View Crossmark data](#)

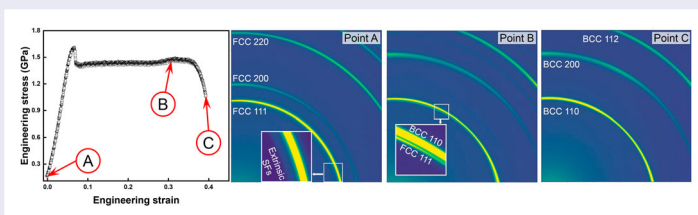
# Overcoming plasticity reduction in a severely deformed nano-grained metastable alloy

Yemao Lu<sup>a,b</sup>, Gaoming Zhu<sup>c,d</sup>, Horst Hahn<sup>a,e</sup> and Yulia Ivanisenko<sup>a</sup>

<sup>a</sup>Institute of Nanotechnology, Karlsruhe Institute of Technology, Karlsruhe, Germany; <sup>b</sup>Karlsruhe Nano Micro Facility (KNMFi), Karlsruhe Institute of Technology (KIT), Eggenstein-Leopoldshafen, Germany; <sup>c</sup>National Engineering Research Center of Light Alloy Net Forming, Shanghai Jiao Tong University, Shanghai, People's Republic of China; <sup>d</sup>Deutsches Elektronen-Synchrotron (DESY), Hamburg, Germany; <sup>e</sup>School of Sustainable Chemical, Biological and Materials Engineering, The University of Oklahoma, Norman, United States

## ABSTRACT

Most bulk metallic materials reveal an increased strength but a loss of ductility after cold deformation, a phenomenon known as the strength–ductility trade-off. In this study, we propose a strategy to overcome this problem by introducing a high density of crystalline defects into a Fe-based metastable alloy by refining grains to a nanometer scale. This procedure effectively enhances the kinetics and reduces the driving force for transformation-induced plasticity (TRIP). Consequently, the TRIP effect originally occurring at cryogenic temperature in the studied alloy becomes active at ambient conditions, contributing to a strength–ductility synergy and overcoming cold working induced sacrifice of ductility.



## IMPACT STATEMENT

High-density crystalline defects were introduced into a metastable alloy, leading to an increase in TRIP temperature. This helps to overcome the strength–ductility trade-off in the severely plastic-deformed alloys at ambient conditions.

## ARTICLE HISTORY

Received 12 March 2024

## KEYWORDS

Metastable alloys;  
transformation-induced  
plasticity; nano grains;  
mechanical properties

## Introduction

High-entropy alloys (HEAs), also named compositional complex alloys (CCAs), have been continuously developed after proposing the primary concept of HEA 20 years ago because of their excellent mechanical performance [1–6]. Apart from the conventional strengthening mechanisms [7–10], some novel strategies to overcome the classic strength–ductility trade-off have been explored in CCAs, such as heterogeneous structures [11], gradient structures [12], transformation-induced plasticity (TRIP) [13], and twinning induced plasticity (TWIP) [14]. Recently, a  $\text{Fe}_{60}\text{Co}_{15}\text{Ni}_{15}\text{Cr}_{10}$  Fe-based metastable CCA with a nearly single face-centered cubic (FCC) phase and minor volume fraction of body-centered

cubic (BCC) has been exploited, which exhibits a tensile strength of  $\sim 1.5$  GPa and a ductility of  $\sim 87\%$  at cryogenic temperatures (77 K). These property combinations are caused by the TRIP effect, the FCC to BCC martensitic transformation [15]. However, this significant TRIP effect is not active over the entire temperature range, leading to a relatively low tensile strength at ambient temperature, caused by the temperature dependence of the free energy difference  $\Delta G^{\text{FCC} \rightarrow \text{BCC}}$  [16].

Subsequently, the  $\text{Fe}_{60}\text{Co}_{15}\text{Ni}_{15}\text{Cr}_{10}$  metastable alloy having a high density of cell dislocations and solute segregation at cell boundaries was fabricated by selective laser melting, which enabled a development of TRIP at ambient temperature, yet accompanied by a minor increase of

**CONTACT** Yemao Lu [yemao.lu@kit.edu](mailto:yemao.lu@kit.edu) Institute of Nanotechnology, Karlsruhe Institute of Technology, Kaiserstr. 12, 76131 Karlsruhe, Germany; Karlsruhe Nano Micro Facility (KNMFi), Karlsruhe Institute of Technology (KIT), 76344 Eggenstein-Leopoldshafen, Germany;  
Gaoming Zhu [zgm900613@sjtu.edu.cn](mailto:zgm900613@sjtu.edu.cn) National Engineering Research Center of Light Alloy Net Forming, Shanghai Jiao Tong University, Shanghai 200240, People's Republic of China; Deutsches Elektronen-Synchrotron (DESY), Hamburg 22607, Germany  
 Supplemental data for this article can be accessed online at <https://doi.org/10.1080/21663831.2024.2356761>.

© 2024 The Author(s). Published by Informa UK Limited, trading as Taylor & Francis Group.

This is an Open Access article distributed under the terms of the Creative Commons Attribution-NonCommercial License (<http://creativecommons.org/licenses/by-nc/4.0/>), which permits unrestricted non-commercial use, distribution, and reproduction in any medium, provided the original work is properly cited. The terms on which this article has been published allow the posting of the Accepted Manuscript in a repository by the author(s) or with their consent.

strength [17]. Moreover, a  $\text{Fe}_{45}\text{Co}_{25}\text{Ni}_{10}\text{V}_{20}$  metastable CCA with a single FCC phase and a tensile strength of 1.1 GPa and a fracture elongation of 82% at 77 K was reported [18]. In this alloy, the phase transformation from FCC to BCC phase occurred predominantly along grain boundaries and increased with strain contributing to the ultimate high strength. Based on the researches on the TRIP effect in austenitic steels and metastable alloys, it is found that the TRIP effect is governed not only by thermodynamic factors such as driving force and temperature but also by the kinetic paths, such as grain boundaries, twin boundaries, dislocation walls and stacking faults (SF), which are essential for providing nucleation sites of the BCC phase formation [15,16,18–22]. Thus, there are promising opportunities to tune the TRIP kinetics in the metastable CCAs by the design of defect structures.

Inspired by these considerations, we aim to increase the density of crystalline defects, mostly grain boundaries, to improve the TRIP  $\text{FCC} \rightarrow \text{BCC}$  kinetic paths. Via this strategy, numerous nucleation sites for the BCC phase transformation will be created providing the possibility to increase the critical temperature for the TRIP effect to occur. To achieve that, the metastable  $\text{Fe}_{60}\text{Co}_{15}\text{Ni}_{15}\text{Cr}_{10}$  CCA is selected to validate our hypothesis because of reports on its interesting mechanical performance after various processes and treatments [22–24]. The alloy was subjected to severe plastic deformation (SPD) process by high-pressure torsion (HPT) [25] to obtain an ultra-fine-grained (UFG) or nano-grained (NG) microstructure. The conventional nanocrystalline materials tend to exhibit limited uniform elongation because of the lack of strain-hardening capability, which is related to the effects of a grain size reduction. This is expected because the extremely small grains cannot store dislocations to increase their density by orders of magnitude as normally possible in coarse-grained (CG) metals [26]. However, this problem can be addressed by the development of the TRIP effect in the NG metastable CCA. As a result, NG structures contribute to a high value of the grain boundary strengthening; simultaneously, the alloy exhibits high ductility due to the TRIP effect. This work opens a new perspective to achieve strength–ductility synergy by creating high density of crystalline defects in metastable alloys. A new concept to tailor the kinetic pathways of metastable alloys by means of grain refinement is proposed.

## Materials and methods

A  $\text{Fe}_{60}\text{Co}_{15}\text{Ni}_{15}\text{Cr}_{10}$  (in the following: Fe60) ingot was produced from pieces of the constituent metals

(purity > 99.9 wt.%) utilizing conventional vacuum arc-melting under argon protective atmosphere. The ingot was inverted and remelted four times with electromagnetic stirring to ensure chemical homogeneity. Subsequently, the samples were homogenized at 1473 K with a heating rate of 115 K/h under a small flow of argon for 6 h followed by furnace cooling. Cold rolling (CR) was conducted with an 88% reduction in thickness (from 9.6 mm to 1.1 mm) after 16 passes. The CR plates were then cut into disks with a diameter of 15 mm, and the disks were heated to 1275 K for 10 min to obtain CG microstructure followed by water quenching. HPT process was performed using CG samples at ambient temperature under a hydrostatic pressure of 6.5 GPa for 5 turns with a rotation speed of 0.5 rpm to obtain an NG structured sample.

Back-scattered electron (BSE) images and electron-backscattered diffraction (EBSD) were conducted using a ZEISS Auriga 60 field emission scanning electron microscope (SEM) with an EBSD detector. Further EBSD analysis was evaluated by orientation imaging microscopy (OIM) software. The samples for SEM and EBSD analyses were mechanically polished using silicon-carbide papers and followed by electropolishing using an electrolyte of 10% perchloric acid and 90% ethanol at  $-5^{\circ}\text{C}$ .

X-ray diffraction measurements were carried out with an Empyrean diffractometer (Malvern Panalytical) operating at 40 kV and 40 mA with  $\text{Cu K}\alpha$  radiation of 0.15406 nm with a step size of  $0.017^{\circ}$ . The beam size was determined as  $2 \times 2 \text{ mm}^2$ .

The transmission electron microscopy (TEM) and automated crystal orientation mapping (ACOM)-TEM measurements were carried out using a ThermoFisher Themis-300 electron microscope at 300 kV equipped with a probe aberration corrector and a Super-X EDX detector. The TEM lamellae were prepared using an FEI Strata 400 equipped with a Gallium focused ion beam (FIB) system and by electropolishing at  $-5^{\circ}\text{C}$  using an electrolyte consisting of 10% perchloric acid and 90% ethanol. The raw ACOM maps with a size of  $500 \times 500$  pixels were recorded with a step size of 2 nm. The pixels with a phase reliability of less than 10 were removed.

Synchrotron X-ray diffraction experiments were carried out at P21.2 beamline, Deutsches Elektronen-Synchrotron (DESY). The X-ray beam, set at an energy of 52.5 keV corresponding to a wavelength of 0.023843 nm, was focused to a size of  $150 \times 150 \mu\text{m}^2$ . Four Varex XRD4343CT area detectors were positioned approximately 2.58 m away based on  $\text{LaB}_6$  calibration. The pyFAI software was employed to integrate the acquired two-dimensional diffraction patterns into one-dimensional diffraction profiles.

Dog-bone-shaped tensile test samples were machined from the HPT disks with a gauge length of 4 mm. Tensile tests were performed at ambient temperature at a strain rate of  $10^{-3} \text{ s}^{-1}$  using a custom-built computer-controlled micro-tensile stage.

## Results

The Fe60 alloy after homogenization shows almost single-phase FCC with only a minor amount of the BCC phase. EBSD phase maps of the CR and CG samples are shown in Figure 1 (a) and (b), respectively. However, the CR sample contains  $\sim 25$  vol.% of BCC phase that has been reported in publication [23], which is attributed to a large amount of strain experienced by the sample during CR. The following heat treatment of the CR sample led to a recrystallization and a reverse transformation from BCC to FCC phase. As a result, the CG sample presents an FCC phase dominated structure with a mean grain size of  $13.7 \pm 9.9 \mu\text{m}$  and a negligible BCC phase amount of 0.2 vol.%. The microstructures of the CG and CR samples are similar to that in the previous reports [23], which were also examined by X-ray diffraction and SEM in the supplementary (Figure S1).

Figure 1 (c–f) shows the microstructures of the NG sample by TEM investigations. The high angular dark field scanning transmission microscopy (HAADF-STEM) image in Figure 1 (c) demonstrates grain size of the NG sample in the range from 20 to 80 nm. The corresponding selected area electron diffraction (SAED) pattern of the NG sample in Figure 1 (d) displays the presence of an NG FCC phase as well as two weak diffraction spots of 200 reflections of the BCC phase indicated by the white circles. Therefore, the HPT deformation apparently had not led to a strain-induced BCC phase formation in NG sample, in contrast to cold-rolling treatment described above. This distinct difference is most likely resulting from the two aspects: (i) the phase transformation from FCC to BCC is accompanied by a lattice expansion and (ii) the HPT was carried out under a pressure of 6.5 GPa in a quasi-hydrostatic condition, which can suppress the volume expansion induced by phase transformation. This effect leads to a reduction of the transformation driving force [27,28].

Additionally, a weak abnormal reflection signal appears inside the FCC (111) ring. The intensity of electron counts along the blue arrow is shown in Figure 1 (d), which could imply a kind of planar fault; extrinsic stacking faults detected using X-ray diffraction method in FCC alloy [29]. Figure 1 (f) represents a high-resolution TEM (HR-TEM) image of NG sample in a [011] zone axis. High-density stacking faults appear in one FCC grain as indicated by white arrows and affirmed using

the Fast Fourier Transforms (FFTs) generated by the selected squares. Simultaneously, it is worth to note the multiple intersections of SF forming networks known as Lomer–Cottrell (LC) locks indicated by white circles.

To support the presence of the high density of defects in the NG sample, we conducted a statistics analysis of stacking fault density from several HR-TEM images and grain boundary density from HAADF images. The analysis reveals a high density of stacking faults, which is approximately  $1.3 \times 10^{16} \text{ m}^{-2}$ . Based on this stacking fault density, the dislocation density can be estimated to be  $2.6 \times 10^{16} \text{ m}^{-2}$ , as typically, a pair of partial dislocations surrounds each stacking fault. The high-angle grain boundary density was also estimated to be  $1.27 \times 10^4 \text{ m/m}^2$ . The outcomes provide a better understanding of the high density of the crystalline defects in the NG sample.

A typical  $60^\circ$  full dislocation consisting of two partial dislocations is shown in supplementary Figure S2 obtained by aberration-corrected STEM image. Moreover, the atomic-resolution HAADF image and corresponding high-resolution energy-dispersive X-ray analysis (EDX) maps of individual elements confirm that no detectable elemental segregation is found at the SFs, as illustrated in Figure S3. In the end, nearly a single FCC phase NG sample containing high density of defects, such as grain boundaries, stacking faults and dislocations, was synthesized successfully.

Figure 2 shows the tensile curves at ambient temperature of the CG, CR and NG samples, respectively. Firstly, it is worth to note that the three samples exhibit completely different mechanical behavior. The CG sample represents a low yield strength of 0.25 GPa, an ultimate tensile strength of 0.54 GPa, and a large total tensile elongation of 0.59, which is comparable to published results [15]. The CR sample reaches a high YS of 1.14 GPa, followed by direct tensile failure without hardening, indicating a typical mechanical performance of cold-deformed alloys [30]. However, a unique tensile behavior appears in the NG sample. The stress–strain curve exhibits pronounced yield point behavior with an ultra-high yield point of 1.61 GPa followed by an abrupt drop of flow stress of approximately 0.2 GPa, resulting in a flow stress of  $\sim 1.4$  GPa. Afterwards, the sample keeps a continuous uniform plastic deformation by a long stress plateau until reaching the strain of 0.23 under the constant stress. Subsequently, the stress–strain curve of the NG sample indicates a slight hardening until a strain of 0.26 where an onset of necking occurred. Finally, the NG sample represented a total elongation of 0.36 after tensile failure. Thus, NG sample demonstrated an excellent combination of strength and elongation. The high YS of the NG sample is mainly attributed to grain boundary strengthening,

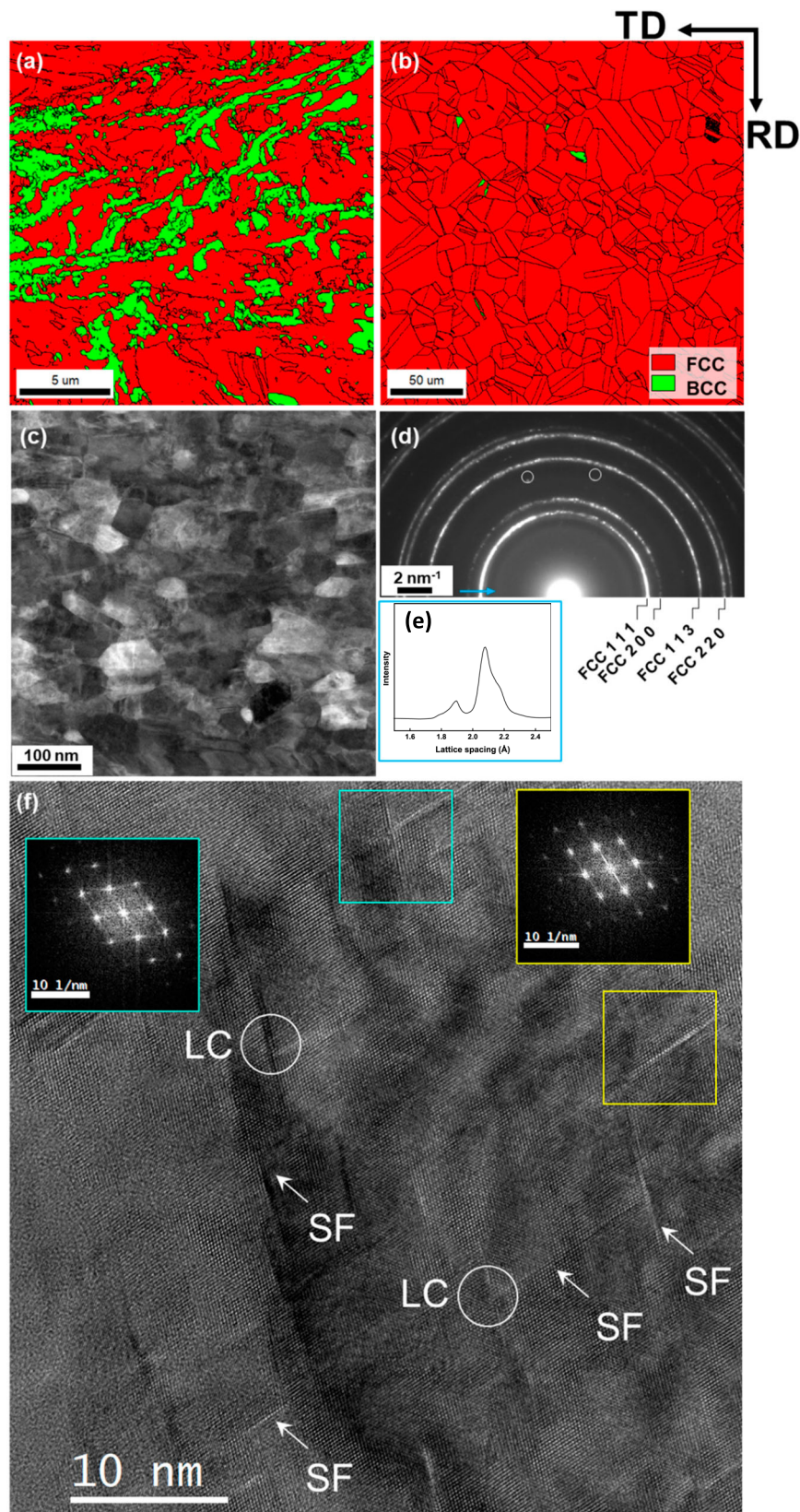


**Figure 1.** Microstructure characterization of the  $\text{Fe}_{60}\text{Co}_{15}\text{Ni}_{15}\text{Cr}_{10}$  alloy in the CR, CG and NG states. (a–b) EBSD phase maps of the CR and CG samples. Black lines indicate high-angle grain boundaries ( $\theta > 15^\circ$ ) (c) HAADF-STEM images of the NG sample. (d) SAED pattern of the NG sample. (e) One-dimensional electron diffraction profiles along blue arrow in (d). (f) HR-TEM image of the NG sample presenting a nano-grain with [011] zone axis. The white arrows indicate SFs, and two Fast Fourier Transforms (FFTs) are from corresponding squares. LC locks are pointed by white circles.

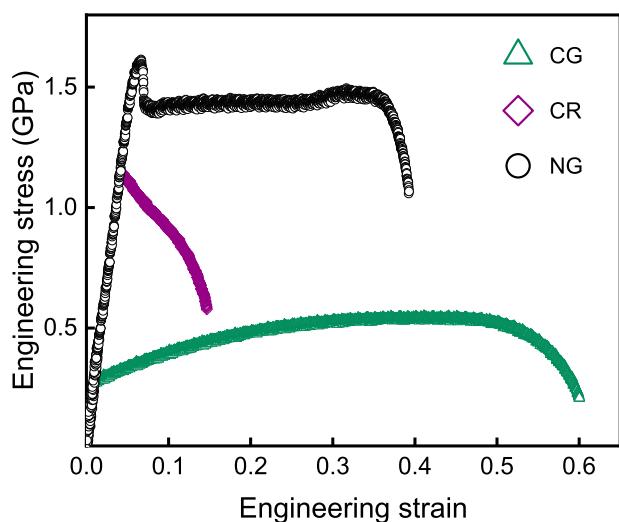


**Figure 2.** Engineering stress–strain curves of the CG, CR and NG samples, respectively. The tensile tests were performed at ambient temperature (293 K).

which is comparable to other single FCC phase CCAs prepared by HPT, e.g.  $\sim 1.7$  GPa in a NG CoCrFeMnNi Cantor alloy with a grain size of  $\sim 50$  nm [31] and 1.66 GPa in a Cantor type NG  $\text{Co}_1\text{Cr}_{0.25}\text{Fe}_1\text{Mn}_1\text{Ni}_1$  alloy with a grain size of 45 nm [32]. Let us note that the yield point behavior followed by an extended stress plateau has been observed in UFG 304 austenitic stainless steel and was related to a development of a Lüders-type deformation due to martensite formation [33].

In order to understand the origin of such a peculiar deformation behavior of the NG sample, the microstructural investigations after tensile fracture at an engineering strain of approximately 0.36 were performed. The HAADF-STEM image in Figure 3 (a) suggests that the grain size distribution is still uniform after deformation with an average grain size of  $\sim 60$  nm, apparently the same as before the tensile test. Remarkably, the SAED pattern in Figure 3 (b) reveals a single BCC phase without

detectable diffraction spots of FCC structure, indicating a full FCC to BCC transformation during the tensile deformation. The phase map from ACOM-TEM in Figure 3 (c) shows that the main phase of the deformed NG sample is the BCC phase without any FCC phase presence. Herein, we conclude that the TRIP behavior of the Fe60 alloy, previously observed at cryogenic temperature (77 K) for the coarse grain structure [17], can be extended to ambient temperature (293 K) for the NG sample. The reason could be the presence of a high density of crystal lattice defects induced by HPT, such as grain boundaries, twin boundaries and stacking faults, which play a critical role for the nucleation of the BCC phase as we proposed.

To evaluate the phase transformation behavior and the micromechanical process of individual phases of the NG sample on a macro scale, synchrotron X-ray diffraction experiments were conducted in the undeformed area (Point A), in the deformed area with an engineering strain of  $\sim 0.26$  corresponding to the onset of necking (Point B) and in the fracture area after strain of 0.36 (Point C), as shown in Figure 4 (a). Figure 4 (b) shows the synchrotron X-ray diffraction patterns of the NG sample at three strain levels. Before the onset of plastic deformation at Point A, virtually only the FCC phase appears in the NG sample. In addition to the diffraction rings of FCC phase, a weak ring inside the 111 ring is also found, which presumably appears due to a presence of extrinsic stacking faults in the FCC structure [29,34]. After intermediate deformation at Point B, the BCC phase dominates in the NC sample, while a small amount of FCC phase remains. The results from the location of the fracture for the NG sample after an engineering strain of 0.36 indicate complete transformation of the FCC phase into the BCC phase. The synchrotron X-ray diffraction results before deformation and at the fracture position are perfectly in agreement with our TEM observations. The two-dimensional diffraction patterns were integrated into one-dimensional diffraction profiles, as shown in Figure 4 (c,d). The dislocation density of the

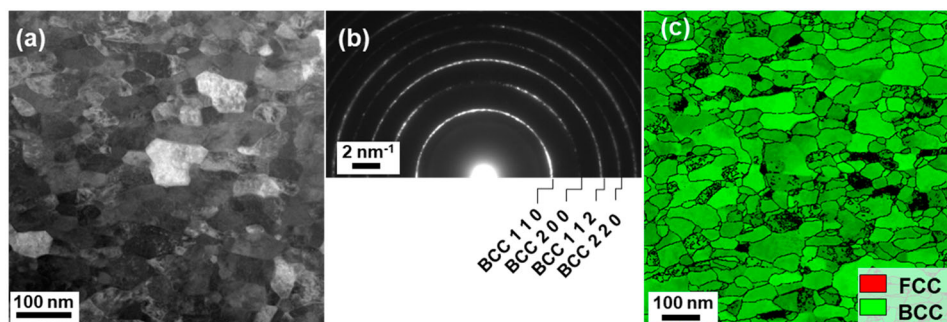


**Figure 3.** TEM investigations on NG specimen after tensile failure near fractured surface with an engineering strain of approximately 0.36. (a) HAADF-STEM image of the NG sample. (b) SAED pattern of the NG sample. (c) Phase map from ACOM-TEM measurement. The pixels where had a phase reliability of less than 10 were removed and the black lines indicate high-angle grain boundaries ( $\theta > 15^\circ$ ).

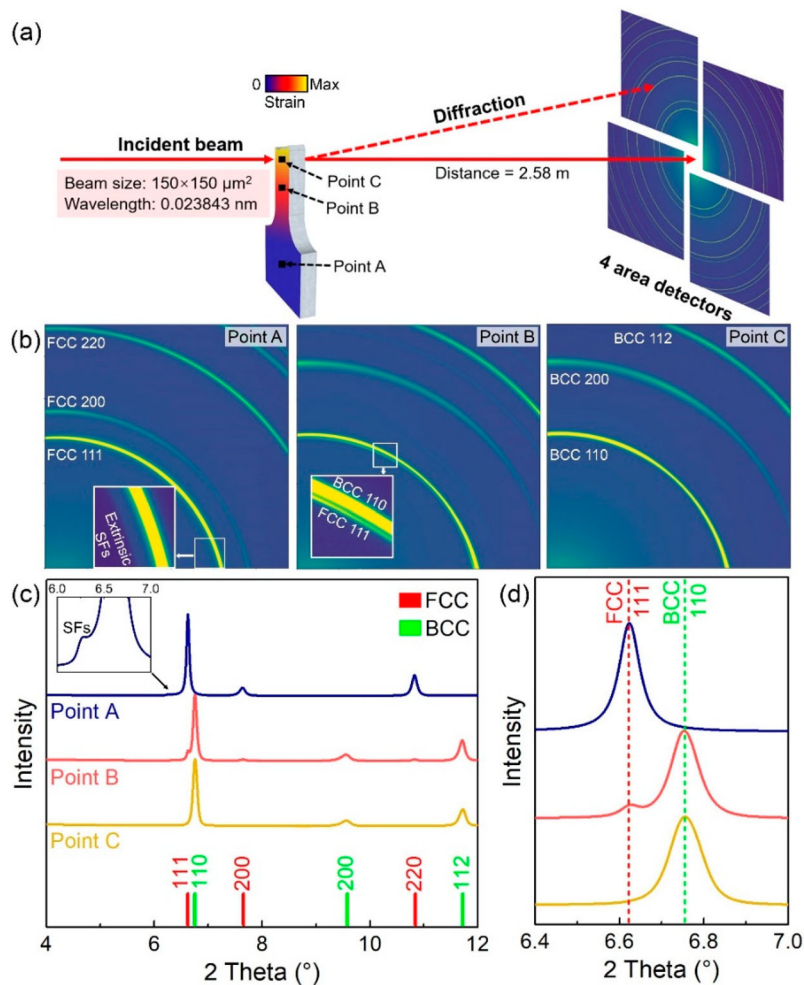


**Figure 4.** Synchrotron X-ray diffraction investigations on a tensile specimen of the NC sample. (a) Schematic of the synchrotron X-ray diffraction experiments; the three measured locations correspond to different strains during the uniaxial tensile deformation, which are 0, 0.26 and 0.36, respectively. (b) Diffraction patterns at three deformation levels; (c, d) one-dimensional diffraction profiles after integration of the data from four area detectors.

NG sample was determined by X-ray line profile analysis using the convolutional multiple whole profile method [35]. The results show that dislocation density in the FCC phase at point A in Figure 4(b) is  $5.9 \times 10^{16} \text{ m}^{-2}$ , whereas the dislocation density in BCC phase at point C is  $4.7 \times 10^{16} \text{ m}^{-2}$ . The measured and fitted patterns are presented in Figure S4.

## Discussion

In this study, we prepared the metastable  $\text{Fe}_{60}\text{Co}_{15}\text{Ni}_{15}\text{Cr}_{10}$  alloy and refined its grain size to the nanoscale ( $< 100 \text{ nm}$ ) using HPT. Additionally, apart from the high density of grain boundaries in the NG sample, large amounts of defects were prompted in the FCC grains as shown in Figure 1 (d–f) and Figure 4 (b–c). The investigations on the deformation-induced FCC to BCC phase transformation reveal that crystal lattice defects

originated from HPT are crucial for promoting nucleation of the BCC phase in fine-grained metastable alloys [15,16,18,20–22]. Hence, the kinetic paths for TRIP effect in the NG sample are dramatically improved, resulting in an occurrence of this effect even at ambient temperature.

The three samples appear to have significantly different strain-hardening behavior. The CG sample shows a high degree of work hardening, which is common for the CG single FCC phase CCAs [36]. This is possible due to deformation twinning, which leads to additional strain hardening which postpones the onset of necking and improves the ductility [37]. The strain–stress curve of the CR sample shows a typical mechanical behavior of cold worked metals. The primary reason for the low ductility is a low strain-hardening capability, which leads to plastic strain instability and early necking [38]. In other words, the increase in density of dislocations during CR hinders further dislocation storage during tensile test, which may

accelerate the plastic flow localization leading to necking at an early stage of tensile deformation [39], resulting in a higher yield strength at the expense of ductility.

The conventional NG and UFG materials tend to lose the work hardening quickly on deformation owing to their very low dislocation storage efficiency inside the tiny grains, especially when in presence of dynamic recovery [40]. Such a high-strength material is therefore prone to plastic instability (early necking), severely limiting the desirable uniform elongation unless larger grains of appropriate sizes and volume fractions are present. However, in our case, the problem can be developed by the TRIP behavior in the NG sample. The TRIP behavior is proposed to start at the upper yield point and continuously occur during the plateau stress deformation stage. Apparently, the triggered phase transformation prevents the development of typical for NG alloys plastic instability (necking) until reaching the strain of 0.23 with a little retained FCC phase, which is comparable to the results from ref [33]. Further tensile deformation-induced slight work hardening until the strain of 0.26 and results in transformation of all the retained FCC phase to the BCC phase, leading to a large ductility of 0.36 after fracture. Nevertheless, detailed explanation of the TRIP mechanism in the NG sample needs further investigation.

We believe that the key role in the development of the TRIP in the NG sample in our study plays the nano-grain structure. The high density of grain boundaries provides numerous nucleation sites for the BCC phase formation, which significantly improves the kinetics paths of the phase transformation. This allows the TRIP effect to occur in the NG sample at ambient temperature. The grain size of the CR sample is of a few micrometers as shown in Figure 1 (b), which is two orders of magnitude larger than that in the NG sample. Therefore, no further phase transformation was observed in the CR sample after tensile experiments as the density of grain boundaries in the CR sample is much less than that in the NG one. It is found that the TRIP effect in austenitic steels and metastable alloys is governed not only by thermodynamic factors such as driving force and temperature but also by the kinetic paths, such as the grain size effect. This grain size effect on TRIP was recently reported in 304 L metastable austenitic steel [41]. In particular, it had been found that the BCC phase nucleated at shear band intersections in samples with large grain size ( $> 34 \mu\text{m}$ ); however, in the UFG sample with a grain size of  $0.5 \mu\text{m}$ , the BCC phase essentially formed on the grain boundaries surprisingly at a lower value of critical strain. This decrease of the critical strain implies the enhanced kinetics of martensitic transformation due to the availability of numerous nucleation sites on the grain boundaries, which is analogous to our results. Hence, it is proposed

that the high density of defects, mostly grain boundaries, significantly improved the kinetic paths for the BCC phase nucleation in the metastable CCAs.

Note also that the high defect density influences the phase equilibrium by decreasing the difference in the Gibbs free energy between the BCC and FCC phases at ambient temperature [28]. The free energy of nanocrystalline alloy after HPT deformation is much higher than that in the coarse-grained state, which increases the FCC to BCC transformation temperature. Furthermore, NG alloys processed by HPT usually contain non-equilibrium grain boundaries and high levels of internal stresses within the crystalline lattice [42], which would also enhance transformation kinetics and contributes to the free energy of the FCC phase.

Eventually, the NG sample exhibits an excellent strength–ductility synergy, which provides an ultra-high strength owing to the nano-scaled microstructure and significantly enhanced plasticity because of TRIP effect. Figure 5 shows a summary of the tensile properties at ambient temperature, i.e. yield strength vs. tensile elongation, of the studied metastable Fe-based NG alloy in comparison with those of other novel CCAs and traditional metallic materials [4,11,13,43–63] Furthermore, the yield point drop phenomenon with continuous long stress plateau in tensile curve of the NG sample during the uniaxial deformation should be explored further as well as its relations with the TRIP effect and Lüders-type deformation.

In summary, a new insight into strength–ductility synergy in metastable alloys is demonstrated. Due to a presence of a high density of grain boundaries and other defects (such as stacking faults) in the nearly single FCC phase NG  $\text{Fe}_{60}\text{Co}_{15}\text{Ni}_{15}\text{Cr}_{10}$  alloy, the critical

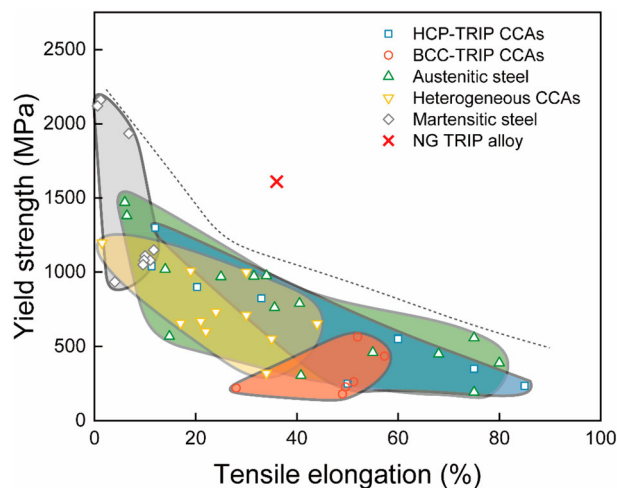


**Figure 5.** Summary of tensile properties at ambient temperature of our NG metastable Fe-based alloy in comparison with some CCAs and conventional steels.

temperature for TRIP occurrence is increased from 77 K for the CG sample to 293 K for the NG sample. The NG sample demonstrates a yield tensile strength of  $\sim 1.61$  GPa and a total elongation of  $\sim 36\%$  at ambient temperature, owing to the synergistic impact of drastic grain refinement and TRIP effect. The strategy of improving transformation kinetics using HPT, resulting in an increase of TRIP temperatures, would be also potentially feasible in other metastable alloys and austenitic steels with TRIP effect to enable them to demonstrate better mechanical performance at ambient temperatures.

## Acknowledgements

This work was partly carried out with the support of the Karlsruhe Nano Micro Facility (KNMFi, [www.knmf.kit.edu](http://www.knmf.kit.edu)), a Helmholtz Research Infrastructure at the Karlsruhe Institute of Technology. We acknowledge DESY (Hamburg, Germany), a member of the Helmholtz Association HGF, for the provision of experimental facilities. Parts of this research were carried out at the PETRA III beamline P21.2. We would like to thank Dr. Alexander Kauffmann for the assistance on the heat treatment and Dr. Ulrich Lienert for the assistance on the synchrotron X-ray experiments.

## Disclosure statement

No potential conflict of interest was reported by the author(s).

## Data availability statement

The data that support the findings of this study are openly available in KITOpen at <https://doi.org/10.35097/1937>, reference number 1000168805.

## References

- [1] Yeh JW, Chen SK, Lin SJ, et al. Nanostructured high-entropy alloys with multiple principal elements: novel alloy design concepts and outcomes. *Adv Eng Mater.* 2004;6:299–303. doi:10.1002/adem.200300567
- [2] Cantor B, Chang ITH, Knight P, et al. Microstructural development in equiatomic multicomponent alloys. *Mater Sci Eng A.* 2004;375–377:213–218. doi:10.1016/j.msea.2003.10.257
- [3] George EP, Curtin WA, Tasan CC. High entropy alloys: a focused review of mechanical properties and deformation mechanisms. *Acta Mater.* 2020;188:435–474. doi:10.1016/j.actamat.2019.12.015
- [4] Li Z, Pradeep KG, Deng Y, et al. Metastable high-entropy dual-phase alloys overcome the strength-ductility trade-off. *Nature.* 2016;534:227–230. doi:10.1038/nature17981
- [5] Wei D, Li X, Heng W, et al. Novel Co-rich high entropy alloys with superior tensile properties. *Mater Res Lett.* 2019;7:82–88. doi:10.1080/21663831.2018.1553803
- [6] Shi P, Ren W, Zheng T, et al. Enhanced strength–ductility synergy in ultrafine-grained eutectic high-entropy alloys by inheriting microstructural lamellae. *Nat Commun.* 2019;10:1–8. doi:10.1038/s41467-019-08460-2
- [7] Hall EO. The deformation and ageing of mild steel: II characteristics of the Lders deformation. *Proc Phys Soc Sect B.* 1951;64:742–747. doi:10.1088/0370-1301/64/9/302
- [8] Petch NJ. The cleavage strength of polycrystals. *J Iron Steel Institution.* 1982;19:8–25.
- [9] Taylor GI. The mechanism of plastic deformation of crystals. part II.—comparison with observations. *Proc R Soc London Ser A* 1934;145:388–404. doi:10.1098/rspa.1934.0107
- [10] Gladman T. Precipitation hardening in metals. *Mater Sci Technol.* 1999;15:30–36. doi:10.1179/026708399773002782
- [11] Jiang Z, Chen W, Chu C, et al. Directly cast fibrous heterostructured FeNi<sub>0.9</sub>Cr<sub>0.5</sub>Al<sub>0.4</sub> high entropy alloy with low-cost and remarkable tensile properties. *Scr Mater.* 2023;230:115421. doi:10.1016/j.scriptamat.2023.115421
- [12] Pan Q, Zhang L, Feng R, et al. Gradient cell-structured high-entropy alloy with exceptional strength and ductility. *Science.* 2021;374:984–989. doi:10.1126/science.abj8114
- [13] Chen S, Oh HS, Gludovatz B, et al. Real-time observations of TRIP-induced ultrahigh strain hardening in a dual-phase CrMnFeCoNi high-entropy alloy. *Nat Commun.* 2020;11:1–8. doi:10.1038/s41467-020-14641-1
- [14] Ding L, Hilhorst A, Idrissi H, et al. Potential TRIP/TWIP coupled effects in equiatomic CrCoNi medium-entropy alloy. *Acta Mater.* 2022;234:118049. doi:10.1016/j.actamat.2022.118049
- [15] Bae JW, Seol JB, Moon J, et al. Exceptional phase-transformation strengthening of ferrous medium-entropy alloys at cryogenic temperatures. *Acta Mater.* 2018;161:388–399. doi:10.1016/j.actamat.2018.09.057
- [16] Olson GB, Cohen M. Kinetics of strain-induced martensitic nucleation. *Metall Trans A.* 1975;6:791–795. doi:10.1007/BF02672301
- [17] Park JM, Asghari-Rad P, Zargaran A, et al. Nano-scale heterogeneity-driven metastability engineering in ferrous medium-entropy alloy induced by additive manufacturing. *Acta Mater.* 2021;221:117426. doi:10.1016/j.actamat.2021.117426
- [18] Li YX, Nutor RK, Zhao QK, et al. Unraveling the deformation behavior of the Fe<sub>45</sub>Co<sub>25</sub>Ni<sub>10</sub>V<sub>20</sub> high entropy alloy. *Int J Plast.* 2023;165:103619. doi:10.1016/j.ijplas.2023.103619.
- [19] Soleimani M, Kalthor A, Mirzadeh H. Transformation-induced plasticity (TRIP) in advanced steels: a review. *Mater Sci Eng A.* 2020;795:140023. doi:10.1016/j.msea.2020.140023
- [20] Venables JA. The martensite transformation in stainless steel. *Philos Mag A J Theor Exp Appl Phys.* 1962;7:35–44. doi:10.1080/14786436208201856
- [21] De AK, Speer JG, Matlock DK, et al. Deformation-induced phase transformation and strain hardening in type 304 austenitic stainless steel. *Metall Mater Trans A.* 2006;37:1875–1886. doi:10.1007/s11661-006-0130-y
- [22] Park JM, Kwon H, Choe J, et al. Cell boundary engineering of ferrous medium-entropy alloy fabricated by laser powder bed fusion. *Scr Mater.* 2023;237:115715. doi:10.1016/j.scriptamat.2023.115715

- [23] Bae JW, Lee J, Zargaran A, et al. Enhanced cryogenic tensile properties with multi-stage strain hardening through partial recrystallization in a ferrous medium-entropy alloy. *Scr Mater.* 2021;194:113653. doi:10.1016/j.scriptamat.2020.113653
- [24] Lee J, Bae JW, Asghari-Rad P, et al. Double-humped strain hardening in a metastable ferrous medium-entropy alloy by cryogenic pre-straining and subsequent heat treatment. *Scr Mater.* 2022;211:114511. doi:10.1016/j.scriptamat.2022.114511
- [25] Valiev RZ, Islamgaliev RK, Alexandrov IV. Bulk nanostructured materials from severe plastic deformation. *Prog. Mater. Sci. Pergamon.* 2000;45:103–189. doi:10.1016/S0079-6425(99)00007-9
- [26] Ma E. Instabilities and ductility of nanocrystalline and ultrafine-grained metals. *Scr Mater.* 2003;49:663–668. doi:10.1016/S1359-6462(03)00396-8
- [27] Patel JR, Cohen M. Criterion for the action of applied stress in the martensitic transformation. *Acta Metall* 1953;1:531–538. doi:10.1016/0001-6160(53)90083-2.
- [28] Ivanisenko Y, MacLaren I, Sauvage X, et al. Shear-induced  $\alpha \rightarrow \gamma$  transformation in nanoscale Fe–C composite. *Acta Mater* 2006;54:1659–1669. doi:10.1016/j.actamat.2005.11.x034
- [29] Balogh L, Ribárik G, Ungár T. Stacking faults and twin boundaries in fcc crystals determined by x-ray diffraction profile analysis. *J Appl Phys.* 2006;100; doi:10.1063/1.2216195
- [30] Povolyaeva E, Shaysultanov D, Astakhov I, et al. Effect of Fe content on structure and mechanical properties of a medium: entropy  $\text{Fe}_x(\text{CoNi})_{100-x}\text{Cr}_9.5\text{C}_0.5$  ( $x = 60$  and  $65$ ) alloys after cold rolling and annealing. *J Alloys Compd.* 2023;959:170469. doi:10.1016/j.jallcom.2023.170469
- [31] Schuh B, Mendez-Martin F, Völker B, et al. Mechanical properties, microstructure and thermal stability of a nanocrystalline CoCrFeMnNi high-entropy alloy after severe plastic deformation. *Acta Mater* 2015;96:258–268. doi:10.1016/j.actamat.2015.06.025
- [32] Lu Y, Mazilkin A, Boll T, et al. Influence of carbon on the mechanical behavior and microstructure evolution of CoCrFeMnNi processed by high pressure torsion. *Materialia.* 2021;16:101059. doi:10.1016/j.mtla.2021.101059
- [33] Mao W, Gao S, Gong W, et al. Quantitatively evaluating the huge Lüders band deformation in an ultrafine grain stainless steel by combining in situ neutron diffraction and digital image correlation analysis. *Scr Mater.* 2023;235:115642. doi:10.1016/j.scriptamat.2023.115642
- [34] Gubicza J, Nauyoks S, Balogh L, et al. Influence of sintering temperature and pressure on crystallite size and lattice defect structure in nanocrystalline SiC. *J Mater Res.* 2007;22:1314–1321. doi:10.1557/jmr.2007.0162
- [35] Ribárik G, Gubicza J, Ungár T. Correlation between strength and microstructure of ball-milled Al–Mg alloys determined by X-ray diffraction. *Mater Sci Eng A.* 2004;387–389:343–347. doi:10.1016/j.msea.2004.01.089
- [36] Gali A, George EP. Tensile properties of high- and medium-entropy alloys. *Intermetallics.* 2013;39:74–78. doi:10.1016/j.intermet.2013.03.018
- [37] Laplanche G, Kostka A, Horst OM, et al. Microstructure evolution and critical stress for twinning in the CrMnFe–CoNi high-entropy alloy. *Acta Mater.* 2016;118:152–163. doi:10.1016/j.actamat.2016.07.038
- [38] Cao Y, Ni S, Liao X, et al. Structural evolutions of metallic materials processed by severe plastic deformation. *Mater Sci Eng R Reports.* 2018;133:1–59. doi:10.1016/j.mser.2018.06.001
- [39] Ovid'ko IA, Valiev RZ, Zhu YT. Review on superior strength and enhanced ductility of metallic nanomaterials. *Prog Mater Sci.* 2018;94:462–540. doi:10.1016/j.pmatsci.2018.02.002
- [40] Wang Y, Chen M, Zhou F, et al. High tensile ductility in a nanostructured metal. *Nature.* 2002;419:912–915. doi:10.1038/nature01133
- [41] Sohrabi MJ, Mirzadeh H, Sadeghpour S, et al. Grain size dependent mechanical behavior and TRIP effect in a metastable austenitic stainless steel. *Int J Plast.* 2023;160:103502. doi:10.1016/j.ijplas.2022.103502
- [42] Zhilyaev AP, Langdon TG. Using high-pressure torsion for metal processing: fundamentals and applications. *Prog Mater Sci.* 2008;53:893–979. doi:10.1016/j.pmatsci.2008.03.002
- [43] Lei C, Deng X, Li X, et al. Mechanical properties and strain hardening behavior of phase reversion-induced nano/ultrafine Fe-17Cr-6Ni austenitic structure steel. *J Alloys Compd.* 2016;689:718–725. doi:10.1016/j.jallcom.2016.08.020
- [44] Xiong Y, He T, Wang J, et al. Cryorolling effect on microstructure and mechanical properties of Fe-25Cr-20Ni austenitic stainless steel. *Mater Des.* 2015;88:398–405. doi:10.1016/j.matdes.2015.09.029
- [45] Hamada AS, Kisko AP, Sahu P, et al. Enhancement of mechanical properties of a TRIP-aided austenitic stainless steel by controlled reversion annealing. *Mater Sci Eng A.* 2015;628:154–159. doi:10.1016/j.msea.2015.01.042
- [46] Xiong Y, Yue Y, Lu Y, et al. Cryorolling impacts on microstructure and mechanical properties of AISI 316 LN austenitic stainless steel. *Mater Sci Eng A.* 2018;709:270–276. doi:10.1016/j.msea.2017.10.067
- [47] Fang TH, Tao NR. Martensitic transformation dominated tensile plastic deformation of nanograins in a gradient nanostructured 316L stainless steel. *Acta Mater.* 2023;248:118780. doi:10.1016/j.actamat.2023.118780
- [48] Seede R, Shoukr D, Zhang B, et al. An ultra-high strength martensitic steel fabricated using selective laser melting additive manufacturing: densification, microstructure, and mechanical properties. *Acta Mater.* 2020;186:199–214. doi:10.1016/j.actamat.2019.12.037
- [49] Lu Q, Eizadjou M, Wang J, et al. Medium-Mn martensitic steel ductilized by baking. *Metall Mater Trans A.* 2019;50:4067–4074. doi:10.1007/s11661-019-05335-5
- [50] Müller T, Kapp MW, Bachmaier A, et al. Ultrahigh-strength low carbon steel obtained from the martensitic state via high pressure torsion. *Acta Mater.* 2019;166:168–177. doi:10.1016/j.actamat.2018.12.028
- [51] Sun J, Jiang T, Wang Y, et al. Effect of grain refinement on high-carbon martensite transformation and its mechanical properties. *Mater Sci Eng A.* 2018;726:342–349. doi:10.1016/j.msea.2018.04.095
- [52] Wu SW, Wang G, Wang Q, et al. Enhancement of strength-ductility trade-off in a high-entropy alloy through a

- heterogeneous structure. *Acta Mater.* 2019;165:444–458. doi:10.1016/j.actamat.2018.12.012
- [53] Zhang C, Zhu C, Harrington T, et al. Design of non-equiatomic high entropy alloys with heterogeneous lamella structure towards strength-ductility synergy. *Scr Mater.* 2018;154:78–82. doi:10.1016/j.scriptamat.2018.05.020
- [54] Chang R, Fang W, Yu H, et al. Heterogeneous banded precipitation of (CoCrNi)<sub>93</sub>Mo<sub>7</sub> medium entropy alloys towards strength-ductility synergy utilizing compositional inhomogeneity. *Scr Mater.* 2019;172:144–148. doi:10.1016/j.scriptamat.2019.07.026
- [55] Zhang C, Zhu C, Cao P, et al. Aged metastable high-entropy alloys with heterogeneous lamella structure for superior strength-ductility synergy. *Acta Mater.* 2020;199:602–612. doi:10.1016/j.actamat.2020.08.043
- [56] Xiong T, Zheng S, Pang J, et al. High-strength and high-ductility AlCoCrFeNi<sub>2.1</sub> eutectic high-entropy alloy achieved via precipitation strengthening in a heterogeneous structure. *Scr Mater.* 2020;186:336–340. doi:10.1016/j.scriptamat.2020.04.035
- [57] Su J, Raabe D, Li Z. Hierarchical microstructure design to tune the mechanical behavior of an interstitial TRIP-TWIP high-entropy alloy. *Acta Mater.* 2019;163:40–54. doi:10.1016/j.actamat.2018.10.017
- [58] Lyu Z, Li Z, Sasaki T, et al. Micromechanical origin for the wide range of strength-ductility trade-off in metastable high entropy alloys<sup>†</sup>. *Scr Mater.* 2023;231:115439. doi:10.1016/j.scriptamat.2023.115439
- [59] Yuan K, Jiang Y, Liu S, et al. Effect of carbon upon mechanical properties and deformation mechanisms of TWIP and TRIP-assisted high entropy alloys. *Mater Sci Eng A.* 2022;857:144126. doi:10.1016/j.msea.2022.144126
- [60] Jo YH, Kim DW, Kim HS, et al. Effects of grain size on body-centered-cubic martensitic transformation in metastable Fe<sub>46</sub>Co<sub>30</sub>Cr<sub>10</sub>Mn<sub>5</sub>Si<sub>7</sub>V<sub>2</sub> high-entropy alloy. *Scr Mater.* 2021;194:113620. doi:10.1016/j.scriptamat.2020.11.005
- [61] Jeong HU, Park N. TWIP and TRIP-associated mechanical behaviors of Fe<sub>x</sub>(CoCrMnNi)<sub>100-x</sub> medium-entropy ferrous alloys. *Mater Sci Eng A.* 2020;782:138896. doi:10.1016/j.msea.2019.138896
- [62] Wang HT, Tao NR, Lu K. Strengthening an austenitic Fe–Mn steel using nanotwinned austenitic grains. *Acta Mater.* 2012;60:4027–4040. doi:10.1016/j.actamat.2012.03.035
- [63] Gu J, Zhang L, Ni S, et al. Effects of grain size on the microstructures and mechanical properties of 304 austenitic steel processed by torsional deformation. *Micron.* 2018;105:93–97. doi:10.1016/j.micron.2017.12.003